JOURNAL OF SOLID STATE CHEMISTRY **126,** 143–151 (1996)
ARTICLE NO. 0322

Determination of Local Geometries around Tellurium in TeO_2–Nb_2O_5 and TeO_2–Al_2O_3 Oxide Glasses by XANES and EXAFS: Investigation of Electronic Properties of Evidenced Oxygen Clusters by *Ab Initio* Calculations

A. Berthereau,* E. Fargin,* A. Villezusanne,* R. Olazcuaga,* G. Le Flem,* and L. Ducasse†

*Institut de Chimie de la Matière Condensée de Bordeaux, Avenue du Docteur A. Schweitzer, 33 605 Pessac; and
†Laboratoire de Physicochimie Théorique, 351, cours de la Libération, 33 405 Talence, France

Received May 16, 1995; in revised form June 10, 1996; accepted June 12, 1996

The origin of the high nonlinear optical response in tellurite glasses is tentatively elucidated from a detailed structural investigation of typical glasses existing in the TeO_2–Al_2O_3 and TeO_2–Nb_2O_5 systems joined to a study of their electronic properties through *ab initio* calculations. As the proportions of Al_2O_3 or Nb_2O_5 increase, the TeO_4 trigonal bipyramids are progressively transformed into a TeO_{3+1} asymetric polyhedron, the geometry of which is actually very close to the TeO_3 trigonal pyramids already found in some crystal structures, e.g., in $ZnTeO_3$. *Ab initio* calculations have been performed on TeO_4 and TeO_3 clusters. The highest occupied molecular orbital is of antibonding type and combines 5*s* AO of tellurium and 2*p* AO of oxygens. The energy difference between this orbitals and the next vacant molecular orbital is lower for the TeO_4 entity than for the TeO_3 cluster. This result is consistent with a higher polarizability of the TeO_4 entity and accordingly with the higher nonlinear index coefficient n_2 of the richest tellurium glasses.

INTRODUCTION

Tellurite glasses are of great scientific interest due to their promising electrical and nonlinear optical properties. The tellurium oxide based glasses exhibit high values of both linear and nonlinear indices, low melting temperature, and wide infrared transmittance (1, 2). Recently nonlinear coefficients n_2 40 times as large as that of SiO_2 have been measured in TeO_2–Nb_2O_5 glasses (3). These exceptional nonlinear properties probably arise from the unique structure of tellurite entities and particularly from the presence of a $5s^2$ electronic lone pair in the electronic configuration (1). A knowledge of the detailed local structure is required to understand the origin of such high nonlinear optical response.

Up to now several experimental techniques (X-ray, Raman spectroscopy, neutron diffraction) have been used to investigate the local structure of tellurite entities (4–6). Three structural TeO_n entities have been reported (Fig. 1): first a TeO_4 somewhat trigonal bipyramid (tbp) group with two axial and two equatorial oxygen atoms (the third equatorial position of the sp^3d hybrid orbitals is occupied by the lone pair); second, a TeO_{3+1} asymmetric polyhedron in which one Te–O axial bond shortens while the other elongates; third, a TeO_3 trigonal pyramid (tp) with three short Te–O distances. TeO_4 and TeO_3 entities look like the tellurium oxygenated environment existing, respectively, in the crystal of α-TeO_2 and $ZnTeO_3$. Therefore these crystalline phases were used as reference samples.

In α-TeO_2 the distorded tbp TeO_4 exhibits two axial Te–O_{ax} bonds (2.08 Å) and two equatorial Te–O_{eq} bonds (1,90 Å) (7), while the Te environment in $ZnTeO_3$ is a tp TeO_3 with a mean Te–O distance equal to 1.876 Å (8).

Besides X-ray techniques, absorption fine structure (XAFS) measurements have been carried out to determine the environment of tellurium in TeO_2–B_2O_3, TeO_2–BaO, and TeO_2–Li_2O–PbO glasses (9–11). The present paper reports a Te–L_{III} edge XANES study and a Te–K edge EXAFS analysis performed on TeO_2–Nb_2O_5 and TeO_2–Al_2O_3 glasses. The structure of these glasses has been already investigated by Raman spectroscopy (3). The Raman spectra exhibited two main peaks at around 640 and 740 cm^{-1}. The relative intensity of the 740 cm^{-1} peak due to TeO_{3+1} units against the 640 cm^{-1} peak intensity due to the TeO_4 tbp increases with Al_2O_3 or Nb_2O_5 content. From these results the addition of an intermediate oxide is assumed to develop the TeO_{3+1} entities.

0022-4596/96 $18.00

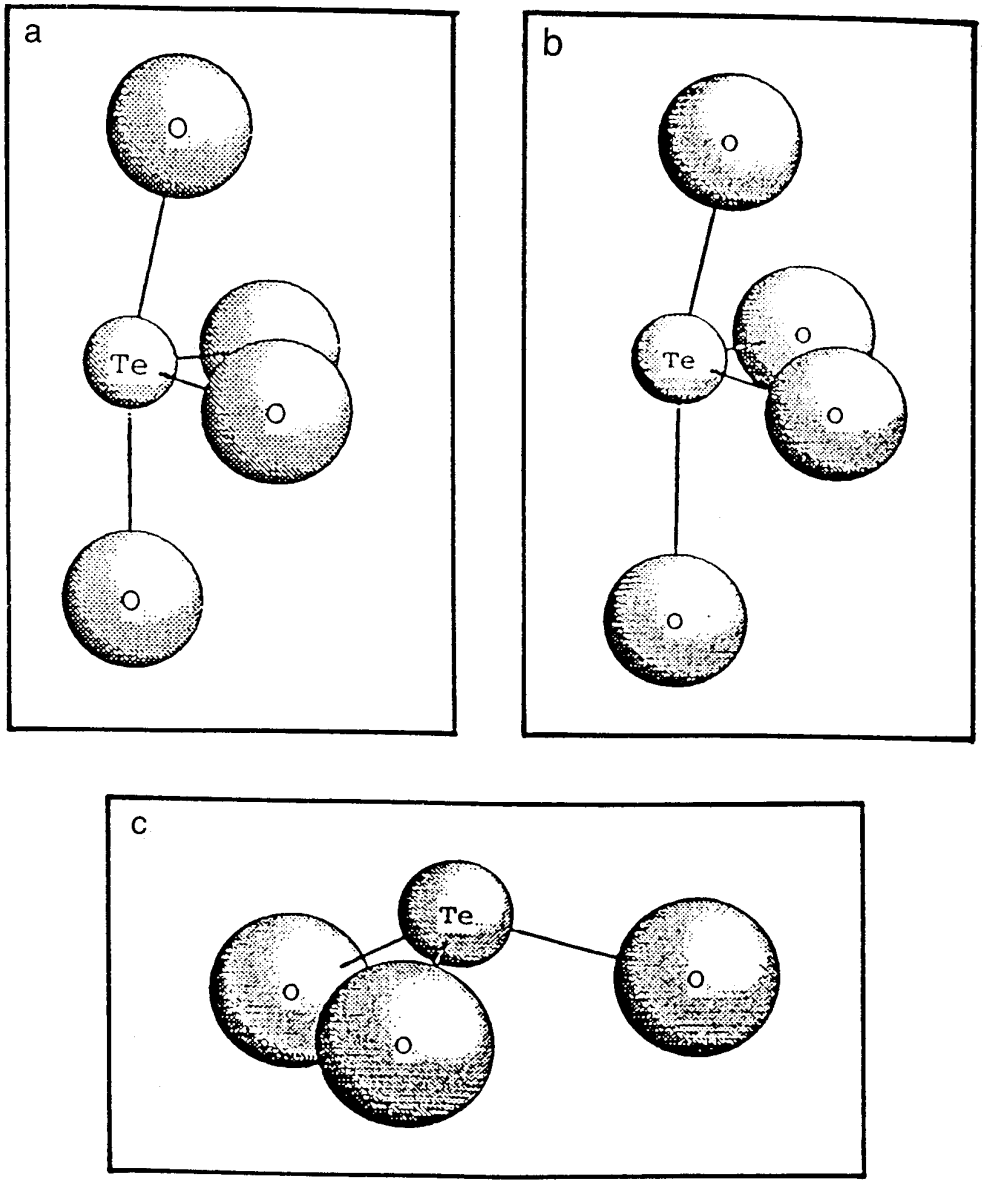

FIG. 1. Illustration of the tellurium atom coordination by oxygen: (a) TeO_4 trigonal bipyramid tbp, (b) TeO_{3+1} polyhedron, (c) TeO_3 trigonal pyramid (tp).

EXPERIMENTAL SECTION AND DATA ANALYSIS

1. Sample Preparation

The compositions of the investigated bulk glasses are $xTeO_2 - (1 - x)\ Nb_2O_5$ and $x\ TeO_2 - (1 - x)\ Al_2O_3$ (with $x = 5$, 10, 15, 20 mol%). Appropriate mixtures of reagent-grade α-TeO_2 (99.995%, Aldrich), Al_2O_3 (99.998%, Koch Light Lab Ltd), and H-Nb_2O_5 (99.998%, Cerac) were melted in a platinum crucible at 950°C for about 30–40 mn in air. These melts were then quenched between two preheated graphite plates and annealed over night at 30°C below their glass transition temperature. The obtained glasses were chemically analyzed with an inductively coupled plasma (ICP) spectrometer. Analyzed compositions are given in Table 1.

Samples for XAFS measurements were prepared by grinding and sieving the glasses to obtain fine powders of homogeneous granulosimetry (20 μm for Te–L_{III} edge and 50 μm for Te–K edge). The mass of glass powder had been previously computed to avoid saturation effects and to optimize the signal-to-noise ratio. Then the powdered glasses were mixed with a convenient ratio of boron nitride

TABLE 1
Nominal and Analyzed Compositions of Some Tellurite Glasses

Nominal compositions	Analyzed compositions
95 TeO_2–5 Nb_2O_5	95.1 TeO_2–4.9 Nb_2O_5
90 TeO_2–10 Nb_2O_5	90.0 TeO_2–10.0 Nb_2O_5
85 TeO_2–15 Nb_2O_5	84.7 TeO_2–15.3 Nb_2O_5
80 TeO_2–20 Nb_2O_5	79.1 TeO_2–20.9 Nb_2O_5
90 TeO_2–10 Al_2O_3	89.9 TeO_2–10.1 Al_2O_3
85 TeO_2–15 Al_2O_3	84.8 TeO_2–14.2 Al_2O_3
80 TeO_2–20 Al_2O_3	82.2 TeO_2–17.8 Al_2O_3

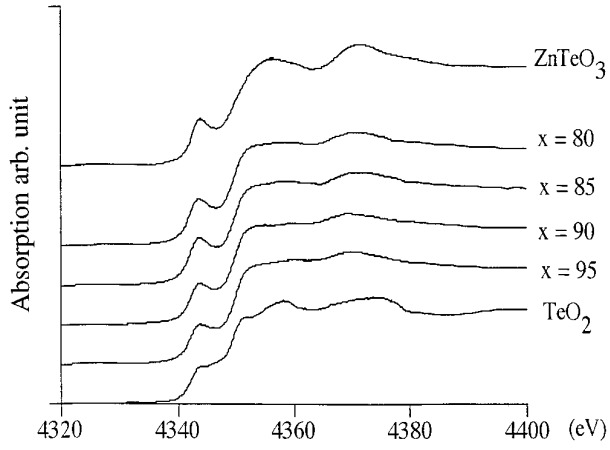

FIG. 2. Te–L_{III} edge XANES spectra of $xTeO_2$–$(1-x)Al_2O_3$ glasses and reference crystals.

powder in order to fill a 1 mm thick and 1 cm^2 surface copper cell sandwiched between two X-ray transparent Kapton adhesive tapes.

2. EXAFS and XANES

2.1. Measurements

Te–K edge XAFS measurements were carried out at LURE (Orsay-France) in transmission mode using the EXAFS III spectrometer. The DCI storage ring used 1.85 GeV positrons with an average intensity of about 150 mA. This station was equipped with a two-crystal Ge(400) monochromator, ensuring a resolution of 25 eV, detuned to discard harmonics from the beam. Two krypton-filled ionization chambers were used to measure the flux intensity before and after the sample. Two scan spectra were recorded for each sample to improve signal-to-noise ratios. Energy steps and counting time were set at 4 eV and 5 s.

Te–L_{III} edge XAFS measurements were carried out in transmission mode at Daresbury SRS Laboratory (Warrington, UK) on the SERC's synchrotron radiation source, using the station 8.1 spectrometer. The two ionization chambers were filled with an Ar–He mixture and a Si(111) double-crystal monochromator was used. Harmonics rejection was obtained by detuning the parallelism of the crystals. The XANES spectra were recorded step by step every 0.2 eV with 5 second accumulation time per point. The resolution can be estimated to be of 1 eV.

2.2. Data Analysis

XANES. The absorption background was first substracted from the experimental spectrum by using a linear function determined by least-square fitting of the pre-edge region. The spectra were then normalized as unit absorbance by taking the midpoint of the first EXAFS oscillation.

EXAFS. The EXAFS analysis was performed following a classical way already described elsewhere (12). The continuous absorption background is estimated by fitting the spectrum before the edge by a linear function, while the main absorption beyond the edge is fitted with an iterative procedure. The resulting EXAFS signal $k\chi(k)$, where k is the photoelectron wave vector, is then normalized. Experimental data between $k_{min} = 3$ Å^{-1} and $k_{max} = 12.5$ Å^{-1} are Fourier transformed in the distance R-space using k^3 ponderation and a Kaiser window (with $\tau = 2.5$). Each peak corresponding to one coordination shell is then filtered and back-transformed to k-space. A single scattering theory permits one to express the resulting signal as a sum of functions. Each shell function depends on k, the wave-vector of the ejected photoelectron, N, the number of atoms in the shell, R, the distance from the absorbing tellurium atoms, σ^2, the Debye–Waller coefficient related to the thermal and static disorder, $\lambda(k)$, the electron mean free path, and $f(k)$ and $\Phi(k)$, the amplitude

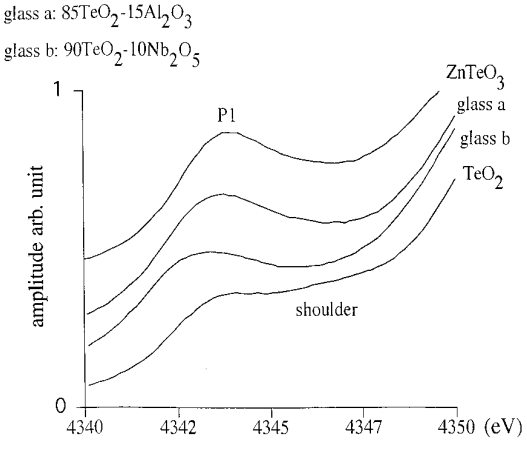

FIG. 3. Zoom on the pre-edge peak.

TABLE 2
Energy Positions and Intensity of the Pre-edge Peak P_1

Sample	Energy position (eV) (±1 eV)	Intensity (±0.02)
$ZnTeO_3$	4343.5	0.47
α-TeO_2	4344.5	0.37
95 TeO_2–5 Nb_2O_5	4344.0	0.37
90 TeO_2–10 Nb_2O_5	4343.5	0.39
85 TeO_2–15 Nb_2O_5	4343.5	0.40
80 TeO_2–20 Nb_2O_5	4343.5	0.44
95 TeO_2–5 Al_2O_3	4344.0	0.40
90 TeO_2–10 Al_2O_3	4344.0	0.41
85 TeO_2–15 Al_2O_3	4344.0	0.46
20 TeO_2–20 Al_2O_3	4343.5	0.46

Note. Peak positions were determined by a derivation method.

and the phase functions for this shell. Structural information can be then extracted by simulations using this function.

Data were obtained using the phase and amplitude parameters tabulated by Teo and Lee (13). For all glasses the EXAFS signal simulations and the number of independent parameters is equal to 5. First the experimental spectra were simulated with only one distance given for each glass, a distance of about 2 Å. In this case a poor agreement between calculated and experimental spectra was observed. Therefore two different Te–O distances were introduced in the first coordination shell. According to the structure of α-TeO_2 all the spectra were fitted with two short Te–O (equatorial) distances and two long (axial) Te–O distances.

Two Debye–Waller factors were introduced, one for each type of distance. The dispersion of Te–O long distances is, in fact, expected to be larger than that of short distances insofar as the two types of Te–O distances are quite different. The total number of neighbors around the tellurium is not allowed to vary and the parameter Γ (equal to $k/\lambda(k)$) is fixed to a mean value of 1.5 $Å^{-2}$. This parameter Γ is deduced from simulations of reference samples α-TeO_2 and $ZnTeO_3$. The edge energy E_o (induced in the k definition) is allowed to vary in order to ensure the transferability of the tabulated Teo and Lee parameters.

3. *Ab Initio* Calculations

Molecular orbital calculations have been performed in the *ab initio* restricted Hartee Fock (RHF) scheme. The GAUSSIAN 92 program which is implemented on the IDRIS (CRAY EC 98-ORSAY) facility was used. The basis set LANLIDZ available on GAUSSIAN 92 was adopted. The valence basis set for tellurium consists of 5*s* and 5*p* double-zeta orbitals. The core orbitals of tellurium atoms are reduced to a frozen orbital effective core potential (ECP), described fully elsewhere by Wadt (14). The clusters TeO_4^{4+} and TeO_3^{2-} were investigated. The molecular orbitals (MO) obtained in RHF calculations were then subsequently used in a configuration interaction (CI) expansion including single and/or double excitations from the Hartree Fock reference.

RESULTS AND INTERPRETATION

1. Te–L_{III} XANES Study

Te XANES spectra of glasses and reference samples (α-TeO_2 and $ZnTeO_3$) are given in Fig. 2.

TABLE 3
Structural Parameters of Optimized and Nonoptimized Geometry of TeO_n^{x-} Clusters and Hartree Fock Energy

Cluster	TeO_4^{4-} [a]	TeO_4^{4-}, optimized	TeO_{3+1}^{4-} [b]	TeO_3^{2-} [c]	TeO_3^{2-}, optimized
Te–O (Å)	1.90 × 2	1.94 × 2	1.88/1.93	1.87 × 3	1.89 × 3
	2.08 × 2	2.14 × 2	1.98/2.41		
O_{eq}–Te–O_{eq} (degree)	101.99	103.70	101.99	99.5 × 2	107.6 × 3
O_{ax}–Te–O_{ax} (degree)	168.51	160.95	168.51	102.5	
O_{ax}–Te–O_{eq} (degree)	86.39 × 2	95.84 × 2	83.38 × 2		
	86.41 × 2	95.88 × 2	86.34 × 2		
E_{HF} (eV)	−8327.1	−8328.3	−8326.8	−6317.2	−6317.5

[a] Parameters extracted from α-TeO_2 structure (7).
[b] Parameters extracted from $Zn_2Te_3O_8$ structure (15).
[c] Parameters extracted from $ZnTeO_3$ structure (8).

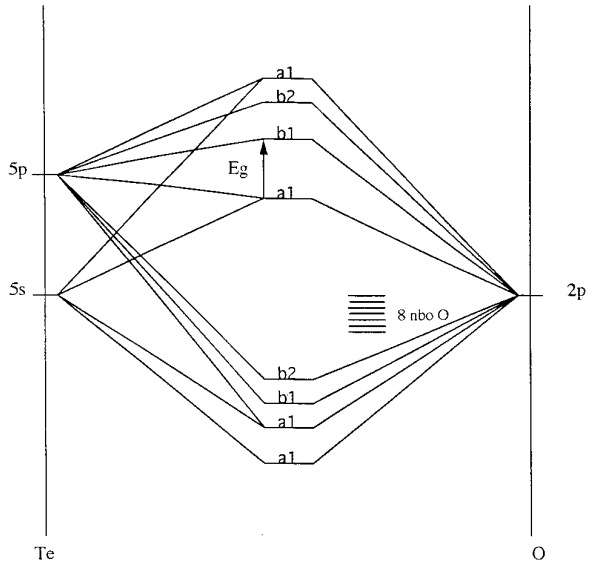

FIG. 4. Qualitative molecular orbital diagram of a TeO_4^{4-} entity. nbo O, nonbonding orbitals of oxygen atom; Eg, energy difference between homo and lumo.

All spectra exhibit pre-edge peaks P_1 whose energy positions are comparable, regarding the resolution of the recordings (Table 2). However a zoom on this pre-edge peak (Fig. 3) shows structural differences depending on the sample. For a $ZnTeO_3$ crystal only one well-defined peak is observed, whereas for α-TeO_2 a quite significant shoulder P_2 appears exactly in the beginning of the slope of the edge, around 3 eV after the maximum of the peak P_1. An intermediate feature is observed for the glasses; this intermediate feature tends to look more and more like a $ZnTeO_3$ peak with increasing Al_2O_3 or Nb_2O_5 content.

This result confirms the conclusions extracted from Raman studies (3), indicating that both TeO_4 and TeO_{3+1} clusters are present in TeO_2–(Al_2O_3 or Nb_2O_5) glasses. Moreover the geometry of the TeO_{3+1} clusters seems to be closer to that of the TeO_3 group of $ZnTeO_3$ when the rate of Al_2O_3 or Nb_2O_5 oxyde increases.

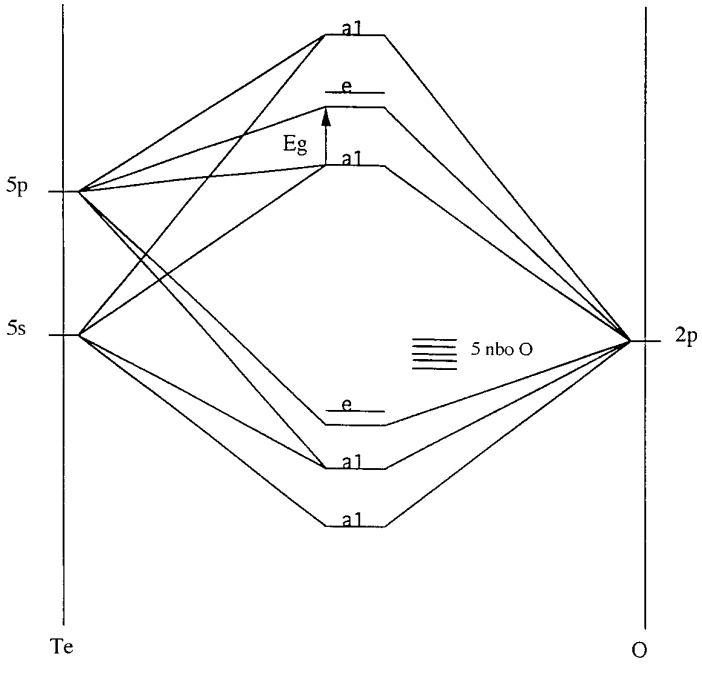

FIG. 5. Qualitative molecular orbital diagram of a TeO_3^{2-} entity. nbo O, nonbonding orbitals of oxygen atom; Eg, energy difference between homo and lumo.

2. *Ab Initio* Results

First, optimization of geometry was performed, giving geometries similar to those which are effectively observed in some tellurite crystals (Table 3). Slight differences were observed for angles which are more opened than in crystals, ensuring a more stable spatial repartition of negative charges in these isolated clusters. Consequently the geometries of clusters TeO_4^{4-} and TeO_3^{2-} found in α-TeO_2 and $ZnTeO_3$ crystals (7, 8), which are close enough to the lowest RHF energies, were adopted as good models to describe tellurium environments in glasses. Besides geometries and RHF energies of TeO_{3+1}^{4-} clusters have been reported in Table 3, giving similar results to those obtained for a TeO_4^{4-} cluster. Optimization of geometry did not converge for such a more complex cluster, probably because the accuracy of RHF energies calculations is not sufficient.

The qualitative molecular orbital diagrams are given in Figs. 4 and 5 for TeO_4^{4-} and TeO_3^{2-} clusters. The conclusions about TeO_{3+1}^{4-} clusters are assumed to be intermediate between those obtained for TeO_3^{2-} and TeO_4^{4-}.

In both case the highest occupied orbital a_1 is of antibonding type and combines essentially 5*s* AO of tellurium and 2*p* AO of oxygens. A large part of this orbital is localized on tellurium and oriented toward the external

TABLE 4
Optical Energy Gap (eV) Obtained by RHF and CI Calculations for TeO_4^{4-} and TeO_3^{2-} Clusters

	TeO_4^{4-}	TeO_3^{2-}
E_g (eV) RHF[a]	10.2	12.1
E_g (eV) CIS[b]	4.4	5.1

[a] Energy difference between homo and lumo states.

[b] Energy difference between the fundamental state and the first excited states.

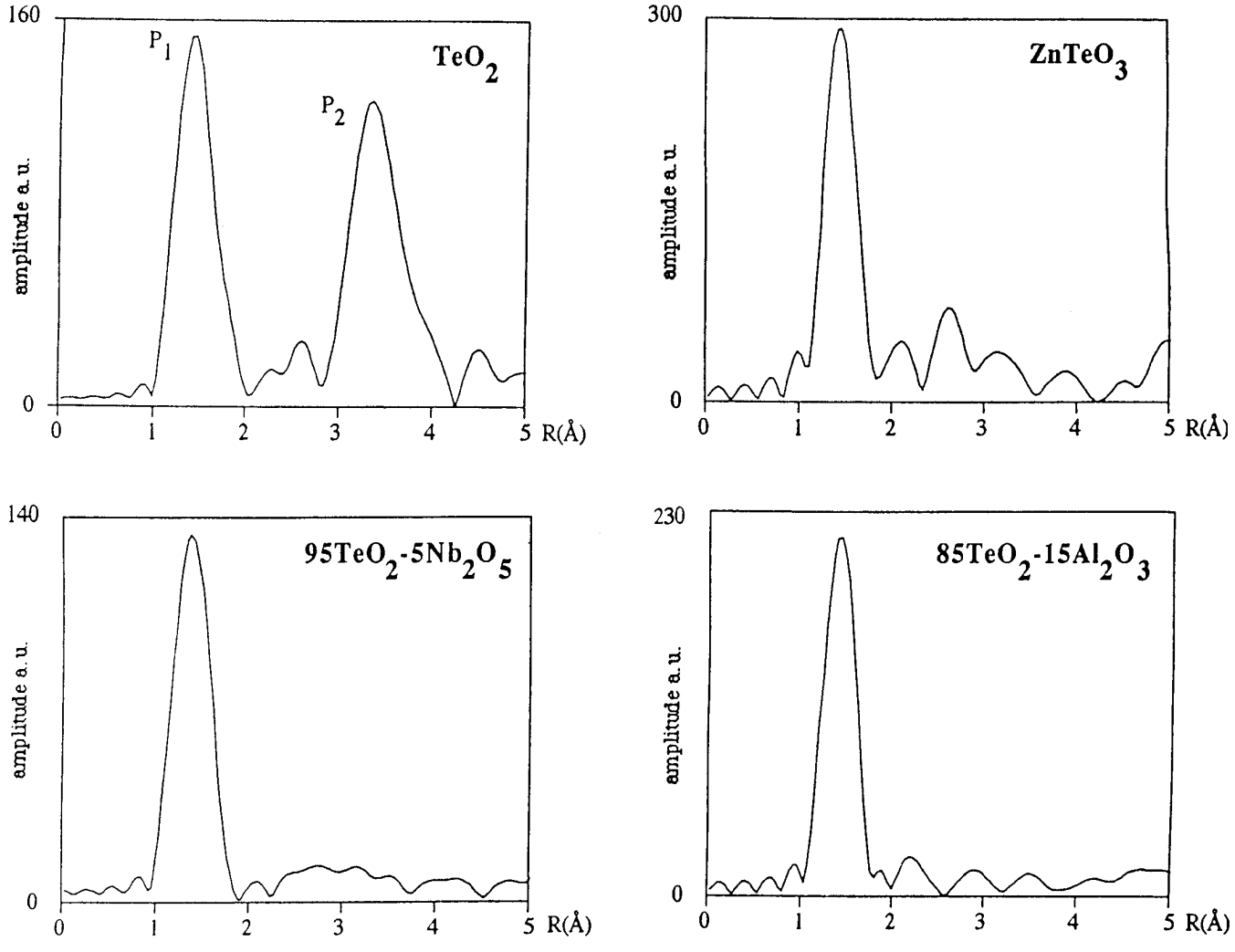

FIG. 6. Fourier transforms of reference samples and some tellurite glasses.

side of the clusters. We can make a correlation between this orbital and the $5s^2$ nonbonding doublet of Lewis (10). The corresponding electrons can be considered as highly polarizable. The polarizability proceeds from an electric field dipolar moment coupling between the occupied molecular orbitals and vacant molecular orbitals. This coupling increases when the energy difference between coupled orbitals decreases. Now *ab initio* calculations show that energy gaps between the last occupied orbital and the three vacant ones are about 1 eV higher for TeO_3^{2-} than for the TeO_4^{4-} cluster, and CI calculations confirm this tendency (Table 4). Therefore we can suppose that the antibonding electron doublet is less polarizable for TeO_3^{2-} than for TeO_4^{4-}.

The three lowest unoccupied antibonding orbitals combine essentially 5*p* AO of tellurium and 2*p* AO of oxygen. In both cases the a_1 MO is the highest in energy and the only one which contains a nonnegligeable fraction of 5*s* AO of tellurium.

All these results allow one to interpret the origin of prepeak P_1 in XANES spectra. This prepeak can effectively be attributed to a $2p_{3/2} \rightarrow 4a_1$ transition, the predominant selection rule of electric dipole transitions $\Delta l = \pm 1$ being fulfilled because of the 5*s* part in the $4a_1$ molecular orbital. However, as *ab initio* calculations do not take into consideration the 5*d* OA of tellurium, which are several eV higher in energy, we can not explain the XANES edge features and particularly the shoulder which is observed in the α-TeO_2 spectrum.

3. Te–K Edge EXAFS Study

We report in Fig. 6 the Fourier transform for the reference samples and some tellurium(IV) oxide glasses.

TABLE 5
Fitting Results for $ZnTeO_3$, α-TeO_2, and Tellurite Glasses

Sample	N	σ^2 (10^{-3} Å^2)	r (Å) (±0.02)	E_0 (eV) (±25)
$ZnTeO_3$	3	0.9	1.89	31 854
α-TeO_2	2	8.1	2.11	31 843
	2	1.6	1.88	
95 TeO_2–5 Nb_2O_5	2	8.1	2.06	31 843
	2	1.6	1.90	
90 TeO_2–10 Nb_2O_5	2	14.4	2.03	31 843
	2	1.6	1.90	
85 TeO_2–15 Nb_2O_5	2	4.9	2.00	31 843
	2	0.9	1.89	
80 TeO_2–20 Nb_2O_5	2	8.1	2.00	31 840
	2	0.9	1.88	
95 TeO_2–5 Al_2O_3	2	8.1	2.07	31 852
	2	0.9	1.90	
90 TeO_2–10 Al_2O_3	2	19.6	2.01	31 853
	2	1.6	1.89	
85 TeO_2–15 Al_2O_3	2	12.1	2.01	31 855
	2	0.9	1.88	

The α-TeO_2 Fourier transform exhibits two peaks (1 and 2) which can be attributed, respectively, to the first oxygen shell around the tellurium and to a second shell corresponding to the first tellurium neighbors.

The Fourier transforms of $ZnTeO_3$ crystal and the whole set of glasses exhibit only one peak which is strong enough to be simulated. This peak can be assigned to the first oxygen shell around tellurium atoms.

All fitted parameters concerning the first oxygen shell around tellurium which are obtained for reference crystals and glasses are summarized in Table 5. Calculated Te–O distances for α-TeO_2 and $ZnTeO_3$ crystals are in fair agreement with the crystallographic data (Table 6) and also prove the reliability of the TeO and Lee amplitude and phase shift parameters.

TABLE 6
Fitting Results for the First and Second Shells of the Reference Samples Compared with Crystallographic Data Extracted from Refs. 7 and 8

Sample	Shell	N	r_{EXAFS} (Å) (±0.02)	r_{CRYST} (Å)
α-TeO_2	1st Te–O	2	2.11	2.082
		2	1.88	1.903
α-TeO_2	2nd Te–Te	2	3.83	3.827
		4	4.08	4.070
		4	3.75	3.740
$ZnTeO_3$	1st Te–O	3	1.89	1.876

In glasses, as the rates of Al_2O_3 and Nb_2O_5 increase the longer Te–O mean distance decreases, whereas the shorter remains approximately constant. The associated Debye–Waller factors have the same magnitude whatever the glass composition and remain comparable to corresponding ones for α-TeO_2 reference. Some fitted spectra are presented in Fig. 7.

4. Discussion

The Raman and XANES experiments indicated the transformation of some TeO_4 entities into TeO_{3+1} entities as the rate of TeO_2 decreases. Therefore the contributions to the signal EXAFS result, for both structural entities, from oxygens at short equatorial distance R_1 in addition to the oxygen of the shortest axial bond R_2' of the TeO_{3+1} entities and to the oxygens of the axial bonds of the TeO_4 bipyramids considered at a mean distance R_2 (Fig. 8).

Assuming the proportions of TeO_4 and TeO_{3+1} clusters are respectively $1 - x$ and x, the number of equatorial distances N_1 is 2 whereas the number of axial distances N_2 is included between 1 and 2, depending on the additional oxide rate and assuming that the elongated axial bond gives an evanescent EXAFS signal. In fact the low accuracy of the EXAFS simulation on the number of atoms in the shell (less than 30% error) as well as the high correlation

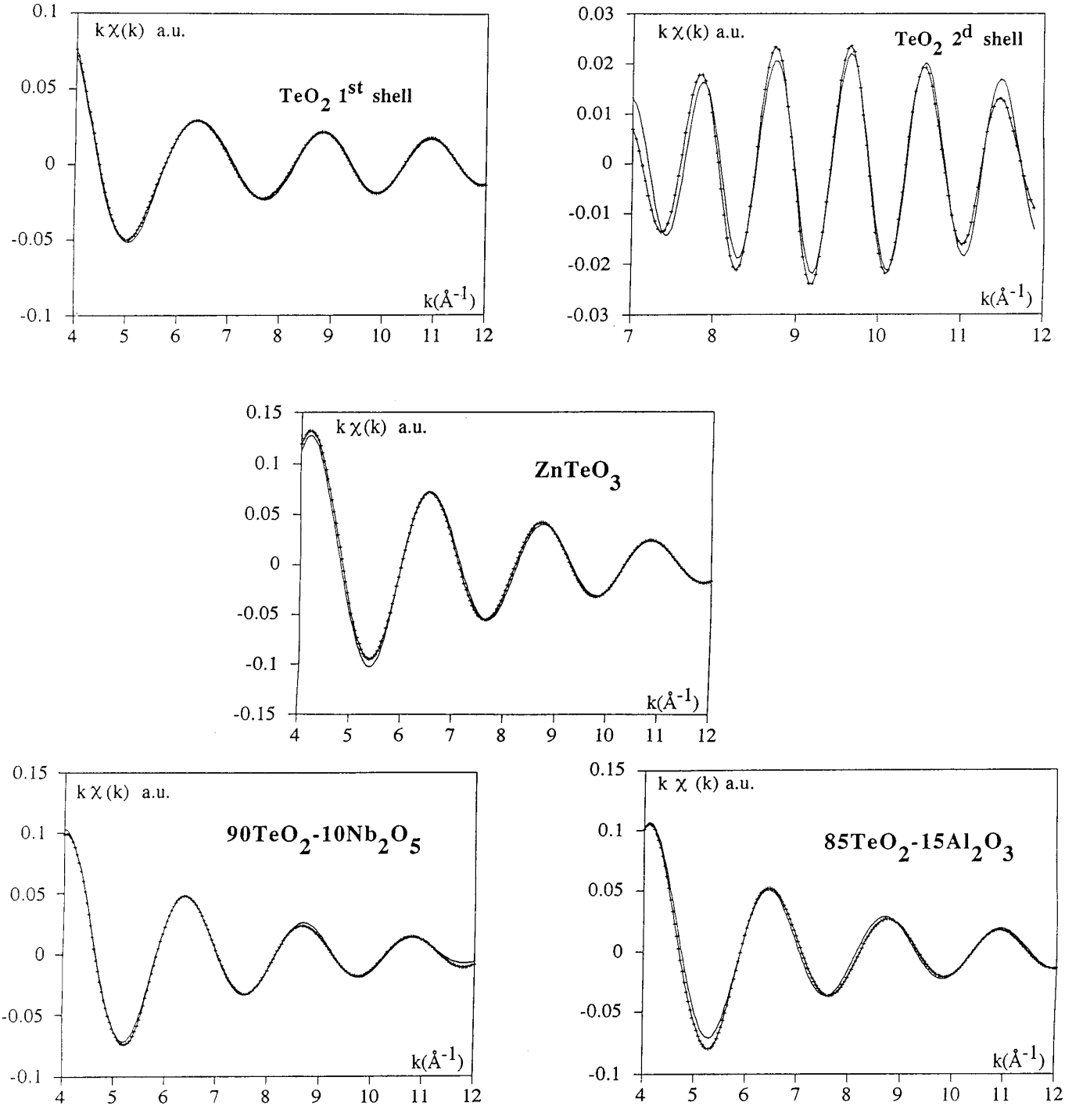

FIG. 7. Experimental and simulated Te–K edge EXAFS spectra of some tellurite glasses and reference samples.

with the Debye–Waller factors exclude a realistic estimation of N_1 and N_2.

CONCLUSION

In the investigated glasses the tellurium environment by oxygen consists of TeO_4 trigonal bipyramid polyhedrons and TeO_{3+1}-type polyhedrons. The addition of Al_2O_3 or Nb_2O_5 increases the proportion of this latter structural entity. Simultaneously a shortening of one axial Te–O bond and an elongation of the other have been deduced from the EXAFS simulations.

Moreover, the detailed analysis of the Te–L_{III} XANES features clearly shows the tendency of the TeO_{3+1} asym-

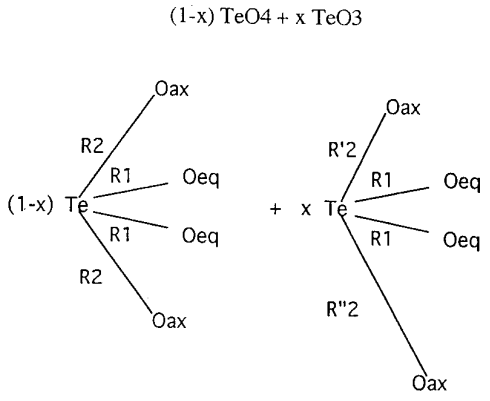

FIG. 8. Transformation of TeO_4 entities into TeO_{3+1} clusters–contributions to EXAFS signal. R1 < R′2 < R2 and R″2 > R2. N1, number of equatorial oxygens, N1 = $2(1 - x) + 2x$. N2, number of axial oxygens, N2 = $2(1 - x) + x$, with distances to tellurium atoms which are less than R2.

metric polyhedrons to adopt the TeO_3 trigonal pyramid geometry. *Ab initio* calculations describing the TeO_4 and TeO_3 clusters indicate the $5s^2$ main character of the highest occupied molecular orbital and allow the attribution of the P_1 prepeak of the XANES spectra to the $2p_{3/2} \rightarrow 4a_1$ transition, where $4a_1$ represents the third vacant molecular orbital. The homo–lumo energy difference is lower for the TeO_4 cluster. Therefore the contribution of such a group to the polarizability, i.e., to the linear and nonlinear index values, is more important than the contribution of the TeO_3 entity. This result is in good agreement with the evolution of both indices, which drastically decrease when the proportion of TeO_2 (3) is diminished and then simultaneously the number of TeO_4 entities in the glass. Further structural investigation by anomalous wide-angle X-ray scattering analysis (AWAXS) is in progress to identify hypothetical short Te–Te distances.

ACKNOWLEDGMENTS

The authors thank LURE and Daresbury SRS Laboratory for provision of Synchrotron Radiation facilities and are grateful to Dr. A. Demourgues for useful suggestions for XANES experiments.

REFERENCES

1. H. Nasu, T. Uchigaki, M. Nakamura, and K. Kamiya, ''Proceedings, International Conference of Science and Technology of New Glasses Tokyo, 1991,'' p. 175.
2. H. Nasu, Y. Ibara, and K. Kubodera, *J. Non-Cryst. Solids* **110,** 229 (1989).
3. A. Berthereau, Y. Le Luyer, R. Olazcuaga, G. Le Flem, M. Couzi, L. Canioni, P. Segonds, L. Sarger, and A. Ducasse, *Mater. Res. Bull* **29**(9), 933 (1994).
4. V. Kozhukharov, H. Bürger, S. Neov, and B. Sidzhimov, *Polyhedron* **5**(3), 771 (1986).
5. T. Sekiya, N. Mochida, A. Ohtsuka, and M. Tonokawa, *J. Non-Cryst. Solids* **144,** 128 (1992).
6. T. Sekiya, N. Mochida, and A. Ohtsuka, *J. Non-Cryst. Solids* **168,** 106 (1994).
7. O. Lindqvist, *Acta Chem. Scand.* **22**(3), 977 (1968).
8. K. Hanke, *Naturwissenschaften* **54**(8), 199 (1967).
9. A. Osaka, Q. Jianrong, T. Nanba, J. Takada, H. Miura, and T. Yao, *J. Non-Cryst. Solids* **142,** 81 (1992).
10. A. Ibanez, T. Ericsson, O. Lindqvist, D. Bazin, and E. Philippot, *J. Mater. Chem.* **4**(7), 1101 (1994).
11. H. Yamamoto, H. Nasu, J. Matsuoka, and K. Kamiya, *J. Non-Cryst. Solids* **170,** 87 (1994).
12. We used the EXAFS data analysis set of programs written in Fortran 77 and implemented by A. Michalowicz (LURE 1985) on the Univac 1110 computer of Paris Sud Informatique at Orsay. The programs are accessible and are available from A. Michalowicz.
13. B. K. Teo, P. A. Lee, A. L. Simons, P. Eisenberg, and B. M. Kinkaid, *J. Am. Chem. Soc.* **99,** 3854 (1977).
14. W. R. Wadt and P. J. Hay, *J. Chem. Phys.* **82**(1), 284 (1985).
15. K. Hanke, *Naturwissenschaften* **53**(11), 273 (1966).